J. Fluid Mech. (2009), *vol.* 640, *pp.* 5–26. © Cambridge University Press 2009
doi:10.1017/S0022112009991029

Estimation of turbulent convection velocities and corrections to Taylor's approximation

JUAN C. DEL ÁLAMO[1] AND JAVIER JIMÉNEZ[2,3]†

[1]MAE Department, University of California San Diego, La Jolla, CA 92093, USA

[2]School of Aeronautics, Universidad Politécnica de Madrid, 28040 Madrid, Spain

[3]Centre for Turbulence Research, Stanford University, Stanford, CA 94305, USA

(Received 15 February 2009; revised 30 June 2009; accepted 30 June 2009; first published online 29 October 2009)

A new method is introduced for estimating the convection velocity of individual modes in turbulent shear flows that, in contrast to most previous ones, only requires spectral information in the temporal or spatial direction over which a modal decomposition is desired, while only using local derivatives in other directions. If no spectral information is desired, the method provides a natural definition for the average convection velocity, as well as a way to estimate the accuracy of the frozen-turbulence approximation. Existing data from numerical turbulent channels at friction Reynolds numbers $Re_\tau \leqslant 1900$ are used to validate the new method against classical ones, and to characterize the dependence of the convection velocity on the eddy wavelength and wall distance. The results indicate that the small scales in turbulent channels travel at the local mean velocity, while large 'global' modes travel at a more uniform speed proportional to the bulk velocity. To estimate the systematic deviations introduced in experimental spectra by the use of Taylor's approximation with a wavelength-independent convection velocity, a semi-empirical fit to the computed convection velocities is provided. It represents well the data throughout the Reynolds number range of the simulations. It is shown that Taylor's approximation not only displaces the large scales near the wall to shorter apparent wavelengths but also modifies the shape of the spectrum, giving rise to spurious peaks similar to those observed in some experiments. To a lesser extent the opposite is true above the logarithmic layer. The effect increases with the Reynolds number, suggesting that some of the recent challenges to the k_x^{-1} energy spectrum may have to be reconsidered.

1. Introduction

Turbulent flows with a dominant velocity component, such as jets or boundary layers, arise in many practical applications. In them, the eddies propagate downstream at a speed that is usually assumed to be close to the local average flow velocity, and which is referred to as the convection velocity (Townsend 1976, ch. 1.7). Its knowledge is often used in laboratory experiments to describe the spatial structure of the flow by applying Taylor's frozen turbulence approximation (Taylor 1938), and is also important in the analysis of turbulence dynamics (Choi & Moin 1990; Kim & Hussain 1993; Krogstad, Kaspersen & Rimestad 1998). Despite its relevance, a complete characterization of the turbulent convection velocity is still lacking for

---

† Email address for correspondence: jimenez@torroja.dmt.upm.es

many flows, because its measurement is arduous both in the laboratory and in simulations. The lack of empirical data is especially serious for the dependence of the convection velocity on eddy size, even if it was shown by Zaman & Hussain (1981) that neglecting that dependence leads to large errors in the interpretation of the large-scale structures in jets. The same is presumably true for other flows, and warnings against the uncritical use of Taylor's approximation (Taylor 1938) appear regularly in the literature. They usually go unheeded, in part for lack of a better alternative. For an excellent introduction to the history of the subject see Zaman & Hussain (1981).

The convection velocity of a generic variable q is usually derived from the frequency–wavenumber spectrum, or from the space–time correlation function, which is its Fourier transform (Willmarth & Wooldridge 1962; Fisher & Davies 1963; Wills 1964). Assume x to be the streamwise direction, the flow to be inhomogeneous along y and homogeneous along x and z. Consider the ω—k_x spectrum $\Phi_q = \langle \widetilde{q}(k_x, k_z, y, \omega)\widetilde{q}^*(k_x, k_z, y, \omega)\rangle$, where $\langle\rangle$ denotes ensemble averaging, ω is the frequency and k_x and k_z are wavenumbers. We use the tilde ($\tilde{}$) to denote the Fourier transform with respect to the two homogeneous directions and time, and the carat ($\hat{}$) for spatial Fourier coefficients that have only been transformed with respect to x and z, but that retain an explicit temporal dependence. Wills (1964) defined the convection velocity of each Fourier mode, $c_{q,1}(k_x, k_z, y)$, as the one maximizing $\Phi_q(k_x, k_z, y, -c_{q,1}k_x)$, which is expressed as

$$\partial_c \Phi_q(k_x, k_z, y, -ck_x)|_{c=c_{q,1}} = 0. \tag{1.1}$$

Alternate definitions in terms of the ω—k_x spectrum are surveyed by Hussain & Clark (1981) and Goldschmidt, Young & Ott (1981). A relatively popular one searches for a maximum along k_x for fixed ω, so that $c_{q,2}(k_x, k_z, y) = \omega(k_x, k_z, y)/k_2$, and

$$\partial k_x \Phi_q(k_x, k_z, y, \omega)|_{k_x=k_2} = 0. \tag{1.2}$$

Comte-Bellot & Corrsin (1971) showed that most definitions are roughly equivalent for low turbulence levels.

The ω—k_x spectrum is conventionally estimated from a space–time series of measurements, $q(x, z, y, t)$, acquired by an array of sensors as described by Capon (1969). The time series from each sensor is divided into segments of N samples that, since they are generally not periodic, are windowed at the edges before performing the Fourier transform. Some segment overlap can be used to recover part of the information lost in this way. The use of the Fourier transform requires the data to be uniformly sampled. If Δt is the sampling rate, the highest (Nyquist) available frequency is $\pi/\Delta t$, while the lowest one, $2\pi/(N\Delta t)$, is determined by the length of the data segments. Turbulent flows are characterized by a wide range of relevant frequencies, so the measurement series used in the computation of the spectrum must be long and finely resolved. The same is true of the sensor arrays used to estimate the spatial spectrum. For these reasons, classical methods for determining convection velocities are very expensive.

The goal of this paper is not to use the results obtained for convection velocity to study the structure of turbulence. Some of the references given above are better sources for that purpose, and our group has already used the new method discussed here to study some aspects of wall-bounded turbulence (Jiménez, del Álamo & Flores 2004; Flores & Jiménez 2006). But the method itself had never been described in detail. In this paper we discuss it, apply it to existing simulation data and use the results to estimate the errors introduced by neglecting the wavelength dependence of the convection velocity when applying Taylor's approximation (Taylor 1938) to turbulent channels. The new method is almost local in either space and time, requiring only, for example, information about the temporal derivative of the spatial spectrum, or about the streamwise derivative of the temporal spectrum. The information needed is purely statistical, and can use data from flow realizations arbitrarily spaced along the direction being differentiated. When applied to simulations, which usually compute the spatial spectra by default, the temporal derivatives can be derived directly from the equations of motion, and provide additional knowledge on how the different terms in the equations contribute to the advection velocities. In experiments, the derivatives can be estimated from two neighbouring spatial or temporal points.

The new method is described in § 2, and related in § 2.1 to earlier methods based on the ω–k_x spectrum. Section 3 validates the new method against older ones, using data from a turbulent channel for which the space–time spectrum was available, and § 4 uses it to study the dependence of the turbulent convection velocities on eddy size, wall-distance and Reynolds number. It is found that the small scales of the flow follow the local mean stream, while the large scales travel at speeds that depend much less on the wall distance, and are roughly proportional to the bulk velocity. Section 5 presents a semi-empirical approximation to the velocities thus found, which is used in § 6 to estimate the effects of Taylor's approximation (Taylor 1938) in channels, and to compute the equivalent uncorrected Taylor one-dimensional (frequency) spectra of the existing simulation data. Interestingly, the resulting spectra contain peaks similar to those that have been observed in some experiments, but which are absent from the wavenumber spectra from which they are derived. Based on the known behaviour of the difference between the bulk and local velocities, the magnitude of the spurious peaks should increase with the Reynolds number. The paper concludes by summarizing the results, including some considerations about the possible implications for some of the recent challenges to the k^{-1} spectral scaling of wall turbulence.

2. Computing convection velocities from local derivatives

This section presents a new method that uses only local time derivatives to calculate turbulent convection velocities from flow realizations arbitrarily spaced in time. We illustrate the method by computing the turbulent convection velocity of the streamwise velocity component (u) in a simulation of an incompressible turbulent shear flow, directly from the Navier–Stokes equations. The spatial Fourier coefficients of u can be written as

$$\widehat{u}(k_x, k_z, y, t) = |\widehat{u}(k_x, k_z, y, t)| \exp[\mathrm{i}\psi_u(k_x, k_z, y, t)], \tag{2.1}$$

where ψ_u is the phase of the complex $\widehat{u}$. We define the average phase velocity of each mode as

$$c_u(k_x, k_z, y) = -\frac{\langle \widehat{u}\widehat{u}^* \partial_t \psi_u \rangle}{k_x \langle \widehat{u}\widehat{u}^* \rangle} = -\frac{\mathrm{Im}\langle \widehat{u}^* \partial_t \widehat{u} \rangle}{k_x \langle |\widehat{u}|^2 \rangle}, \tag{2.2}$$

which is exact for a monochromatic frozen wave proportional to $\exp[\mathrm{i}k(x - ct)]$.

An alternative way of deriving this expression, which is valid for more general situations, is to find the value of c which minimizes the difference between the real time evolution of $u(x, t)$, and a frozen wave $u(x - ct)$. If we express this problem as the minimization of the square of the total derivative,

$$1-\gamma^2 \equiv \frac{\langle(\partial_t u + c\partial_x u)^2\rangle}{\langle(\partial_t u)^2\rangle}, \tag{2.3}$$

we obtain

$$C_u = -\frac{\langle\partial_t u\,\partial_x u\rangle}{\langle(\partial_x u)^2\rangle} \tag{2.4}$$

and an optimal value for γ,

$$\gamma_u = \frac{|\langle\partial_t u\,\partial_x u\rangle|}{[\langle(\partial_t u)^2\rangle\langle(\partial_x u)^2\rangle]^{1/2}}. \tag{2.5}$$

The coefficient γ_u is a figure of merit for the frozen-turbulence approximation, which is nothing but the correlation coefficient between the spatial and temporal derivatives. It equals unity for a perfect frozen wave, and zero for eddies that decay or deform too fast to travel coherently across a wavelength. When u contains a single Fourier mode, (2.4) is equivalent to (2.2), and

$$\gamma_u(k_x, k_z, y) = \frac{|\mathrm{Im}\langle\widehat{u}^*\partial_t\widehat{u}\rangle|}{[\langle|\partial_t\widehat{u}|^2\rangle\langle|\widehat{u}|^2\rangle]^{1/2}}. \tag{2.6}$$

For more general cases in which the velocity is expressed as a Fourier expansion over a range Ω of wavenumbers, (2.4) provides a natural definition for the overall convection velocity associated with Ω, which can be expressed as

$$C_u(y) = \frac{\displaystyle\int_\Omega c_u(k_x, k_z, y)|\widehat{u}(k_x, k_z, y)|^2\,k_x^2\,\mathrm{d}k_x\,\mathrm{d}k_z}{\displaystyle\int_\Omega |\widehat{u}(k_x, k_z, y)|^2\,k_x^2\,\mathrm{d}k_x\,\mathrm{d}k_z}, \tag{2.7}$$

and, likewise,

$$\gamma_u(y) = C_u(y)\left[\frac{\displaystyle\int_\Omega |\widehat{u}(k_x, k_z, y)|^2\,k_x^2\,\mathrm{d}k_x\,\mathrm{d}k_z}{\displaystyle\int_\Omega |\partial_t\widehat{u}(k_x, k_z, y)|^2\,\mathrm{d}k_x\,\mathrm{d}k_z}\right]^{1/2}. \tag{2.8}$$

Note that (2.2) and (2.7) weight the instantaneous phase velocity with the energy, so that stronger events contribute more than weaker ones. Mean convection velocities $C_{u,1}(y)$ and $C_{u,2}(y)$ can be similarly generated from the two spectral definitions (1.1) and (1.2).

The numerator in the rightmost member of (2.2) can be obtained in any suitable way, but in simulations it is easier to obtain it directly from the equations of motion. Write the u-momentum equation as

$$\partial_t\widehat{u} + \mathrm{i}k_x U\widehat{u} + \widehat{F_u} + \widehat{v}\partial_y U = -\mathrm{i}k_x\widehat{p} + \nu\left(\partial_{yy}^2 - k_x^2 - k_z^2\right)\widehat{u}, \tag{2.9}$$

where $U(y)$ is the mean velocity profile, p is the kinematic pressure, ν is the kinematic viscosity and $\widehat{F_u}$ is the Fourier transform of the nonlinear terms. It follows that

$$\mathrm{Im}[\widehat{u}^*\partial_t\widehat{u} + \widehat{F_u}\widehat{u}^* + \widehat{v}\widehat{u}^*\partial_y U] + k_x U\widehat{u}\widehat{u}^* = -k_x\mathrm{Re}(\widehat{p}\widehat{u}^*) + \nu\,\mathrm{Im}\left[\widehat{u}^*\partial_{yy}^2\widehat{u}\right]. \tag{2.10}$$

Combining (2.2) and (2.10), we obtain

$$c_u(k_x, k_z, y) = U(y) + \frac{k_x\mathrm{Re}\langle\widehat{p}\widehat{u}^*\rangle + \mathrm{Im}\left[\langle\widehat{F_u}\widehat{u}^*\rangle + \langle\widehat{v}\widehat{u}^*\rangle\partial_y U - \nu\langle\widehat{u}^*\partial_{yy}^2\widehat{u}\rangle\right]}{k_x\langle\widehat{u}\widehat{u}^*\rangle}, \tag{2.11}$$

where it is straightforward to identify the contribution from each term in the equations of motion. Note that the viscous terms in the homogeneous directions do not contribute to the convection velocity, and that (2.11) only contains averaged quantities, which can be determined without the need of sampling data with a uniform time resolution. The convection velocities of v and w are given by similar expressions,

$$c_v(k_x, k_z, y) = U(y) + \frac{\operatorname{Im}\left[\langle \widehat{v}^* \partial_y \widehat{p}\rangle + \langle \widehat{F_v}\widehat{v}^*\rangle - \nu\langle \widehat{v}^* \partial^2_{yy}\widehat{v}\rangle\right]}{k_x\langle \widehat{v}\widehat{v}^*\rangle}, \tag{2.12}$$

$$c_w(k_x, k_z, y) = U(y) + \frac{k_z \operatorname{Re}\langle \widehat{p}\widehat{w}^*\rangle + \operatorname{Im}\left[\langle \widehat{F_w}\widehat{w}^*\rangle - \nu\langle \widehat{w}^* \partial^2_{yy}\widehat{w}\rangle\right]}{k_x\langle \widehat{w}\widehat{w}^*\rangle}, \tag{2.13}$$

which lack explicit contributions from the mean shear $\partial_y U$. Convection velocities for the vorticity fluctuations can be determined using the same procedure.

2.1. *The relation to spectral methods*

Equation (2.2) is closely related to the methods based on the full ω–k_x spectrum. Consider the temporal Fourier transform $\widetilde{u}(k_x, k_z, y, \omega)$ of the spatial coefficient $\widehat{u}(k_x, k_z, y, t)$. The Fourier transform of $\partial_t \widehat{u}$ is $\mathrm{i}\omega\widetilde{u}$, and it follows from Parseval's theorem that

$$\langle \widehat{u}^* \partial_t \widehat{u}\rangle = \mathrm{i}\int_{-\infty}^{\infty} \omega \Phi_u(k_x, k_z, y, \omega)\,\mathrm{d}\omega, \tag{2.14}$$

and

$$\langle \widehat{u}^* \widehat{u}\rangle = \int_{-\infty}^{\infty} \Phi_u(k_x, k_z, y, \omega)\,\mathrm{d}\omega, \tag{2.15}$$

so that (2.2) becomes

$$c_u = -\frac{1}{k_x}\frac{\displaystyle\int_{-\infty}^{\infty} \omega \Phi_u(k_x, k_z, y, \omega)\,\mathrm{d}\omega}{\displaystyle\int_{-\infty}^{\infty} \Phi_u(k_x, k_z, y, \omega)\,\mathrm{d}\omega}. \tag{2.16}$$

The new phase velocity is then defined by the position of the centre of gravity of the ω-spectrum at a given wavenumber, instead of by its maximum.

A similar definition, useful for laboratory experiments, can be derived for temporal data series. For example, $\langle \overline{u}^* \partial_x \overline{u}\rangle$, where $\overline{u}(x, k_z, y, \omega)$ is a Fourier coefficient transformed with respect to time but not to x, is the transform of the correlation $\langle u(t')\partial_x u(t'+t)\rangle$, which can be determined experimentally by estimating $\partial_x u$ from two neighbouring probes.

The dual of (2.2) is

$$c'_u(k_z, y, \omega) = -\frac{\omega\langle \overline{u}^* \overline{u}\rangle}{\operatorname{Im}[\langle \overline{u}^* \partial_x \overline{u}\rangle]}, \tag{2.17}$$

which is equivalent to

$$c'_u = -\omega\frac{\displaystyle\int_{-\infty}^{\infty} \Phi_u(k_x, k_z, y, \omega)\,\mathrm{d}k_x}{\displaystyle\int_{-\infty}^{\infty} k_x \Phi_u(k_x, k_z, y, \omega)\,\mathrm{d}k_x}. \tag{2.18}$$

The two phase velocities, c_u and c'_u, are not strictly equivalent to each other, and neither of them are equivalent to the velocities $c_{u,1}$ and $c_{u,2}$ defined in the introduction,

Case	Re_τ	L_x/h	L_z/h	Δx^+	Δz^+	N_y	Tu_τ/h	N_F
L180	185	12π	4π	14	6.8	97	50	106
L550	547	8π	4π	13	6.7	257	20	142
L950	934	8π	3π	11	5.7	385	12	74
S1900	1901	π	$\pi/2$	12	5.8	769	7.4	94

Table 1. Parameters of the simulations. L_x and L_z are the streamwise and spanwise dimensions of the computational box, and h is the channel half-width. Δx and Δz are resolutions in terms of Fourier modes. N_y is the number of Chebychev polynomials. T is the time during which the statistics were collected after discarding initial transients, u_τ is the friction velocity and N_F is the number of instantaneous flow realizations used to compute convection velocities.

but c_u is related to $c_{u,1}$, while c'_u is closer to $c_{u,2}$. All the definitions are equivalent for a frozen monochromatic wave whose spectrum is proportional to a Dirac's delta $\Phi_u(k_x, \omega) \sim \delta(k_x - k_0)\delta(\omega - ck_0)$, with arbitrary k_0.

3. Validation of the new scheme

We next apply the procedure in §2 to compute convection velocities from ensembles of instantaneous flow realizations of direct numerical simulations of plane turbulent channels with $180 \leqslant Re_\tau = hu_\tau/\nu \leqslant 1900$, where h is the channel half-width and u_τ is the friction velocity. Their parameters are summarized in table 1, and they were documented in del Álamo & Jiménez (2003) and del Álamo *et al.* (2004, 2006). Variables in wall units, normalized with u_τ and ν, are denoted by superscript +.

To validate the new procedure, we also calculate convection velocities for the L550 channel using the two conventional definitions based on the spectral maxima, (1.1) and (1.2). The ω–k_x spectra for L550 were obtained as described in the introduction, using 18 temporal data segments with $N = 1024$ samples, and a Hanning window with 50 % overlap, yielding a frequency range $0.14 \leqslant h|\omega|/U_b \leqslant 71$. To save storage, we only recorded time series for Fourier modes satisfying $\lambda_x, \lambda_z \geqslant 0.25h = 137\nu/u_\tau$, which however represent more than 75 % of the turbulent kinetic energy above $y^+ = 100$, and 55 % at $y^+ = 15$ (del Álamo & Jiménez 2002). Wavelengths are defined as $\lambda = 2\pi/k$.

The results from the three definitions, integrated over the wavenumber range just mentioned, are compared in figures 1(*a*) and 1(*b*) for the streamwise and wall-normal velocities. They collapse almost perfectly in the outer region. The agreement is worse near the wall, which is not unexpected, since there is where the turbulence intensity and the mean shear are largest, and the turbulent structures are expected to deviate more from frozen waves.

A more sensitive indicator is the spectral distribution of the convection velocities obtained with the different methods. These are compared in figures 2(*a*) and 2(*b*), which display deviations from the local mean velocity, $\Delta c(\lambda_x, y) = c(\lambda_x, y) - U(y)$, at three different wall distances. As in figures 1(*a*) and 1(*b*), the averaging at each λ_x is restricted to spanwise wavelengths $\lambda_z \geqslant 0.25h$, to match the range in which ω–k_x spectra were available.

Again the agreement is good, in particular away from the wall, and for the shorter wavelengths. The largest deviations from the mean profile are found near the wall, as well as the largest discrepancies between the two spectral definitions, but even

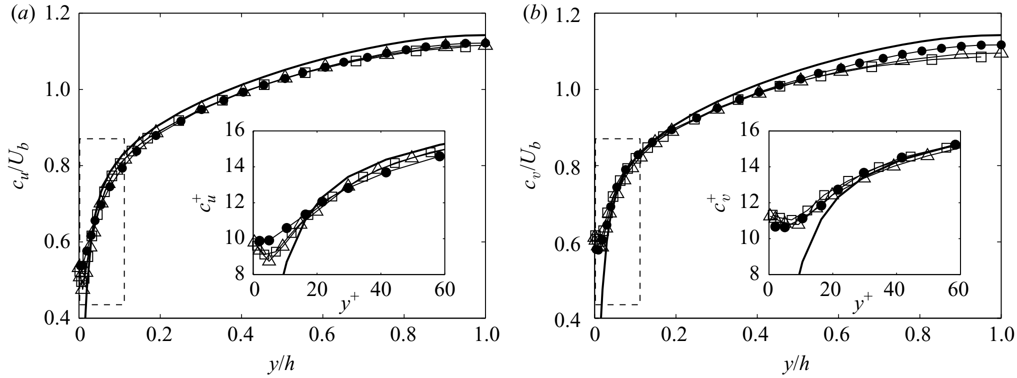

FIGURE 1. Mean turbulent convection velocity profiles of the streamwise and wall-normal velocity, averaged using (2.7), and plotted as a function of the wall distance y. Case L550. Only those Fourier modes with $\lambda_x, \lambda_z \geqslant 0.25h$ are considered: ——, mean velocity profile $U(y)$; —●—, present method, (2.11) and (2.12). Open symbols come from conventional definitions based on the ω–k_x spectrum, —□—, C_1 (1.1); —△—, C_2 (1.2). The insets are enlargements of the framed regions of each panel, in wall units: (*a*) $C_u(y)$. (*b*) $C_v(y)$.

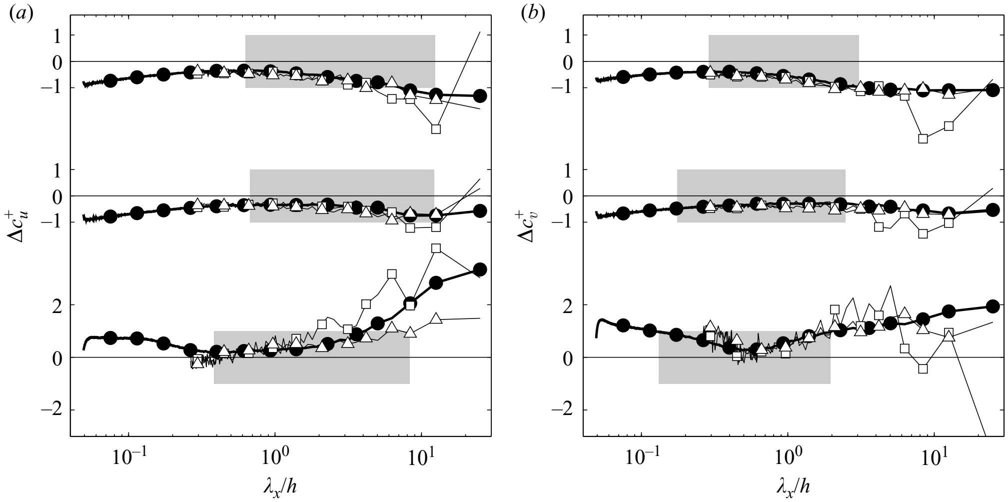

FIGURE 2. Spectral distribution of the difference Δc between the convection velocity and the mean profile, represented as a function of the streamwise wavelength, λ_x. Case L550 at (from bottom to top) $y/h = 0.02$, 0.2, 0.75 ($y^+ = 10$, 100, 410). Only those Fourier modes with $\lambda_z \geqslant 0.25h$ are considered. Open symbols come from conventional definitions based on the ω–k_x spectrum: —□—, Δc_1 (1.1); —△—, Δc_2 (1.2). The shaded patches show the wavelength interval around the peak of the spectral energy density of u and v that contains 3/4 of the total energy at each wall distance: (*a*) Δc_u, (*b*) Δc_v.

there the three definitions agree within the apparent experimental scatter. Note that the results of the two spectral definitions are quite scattered for long wavelengths, probably due to the difficulty of identifying maxima in that noisier part of the ω–k_x spectrum. The new definition, which is based on a statistical average, provides smoother data everywhere. For the rest of this paper we will use c_u as our only definition of the convection velocity.

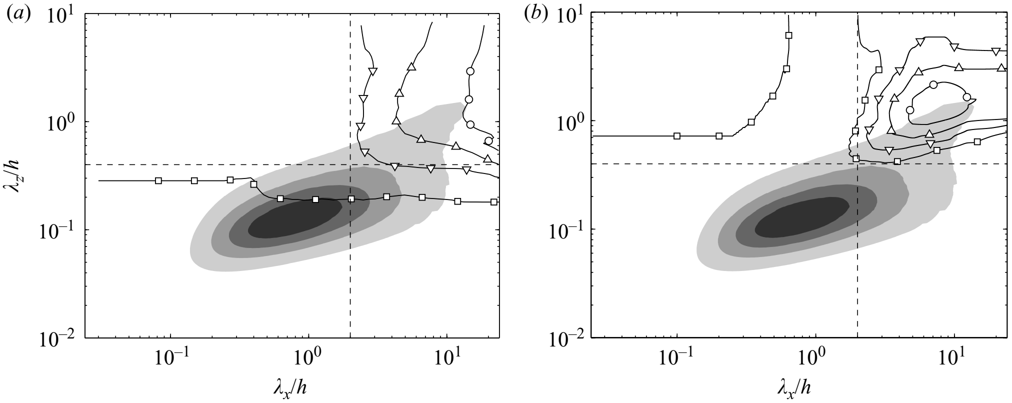

FIGURE 3. Contour plot of the two-dimensional spectral distribution of (*a*) the convection velocity of u, and (*b*) its coherence coefficient γ_u, as functions of the streamwise and spanwise wavelengths. Case L950 at $y^+ = 15$ ($y = 0.016h$, $U^+ = 10.7$). The contour lines in (*a*) are, □, $c_u^+ = 11$; ▽, 13; △, 15; ○, 17. In (*b*), they are □, $\gamma_u^+ = 0.3$; ▽, 0.4; △, 0.5; ○, 0.6. The shaded contours are linearly equispaced isolines of the two-dimensional energy density of the streamwise velocity at the same wall distance. The horizontal and vertical dashed lines correspond respectively to $\lambda_z = 0.4h$ and $\lambda_x = 2h$, and are included for reference.

4. Spectral and spatial dependence of the convection velocity

Besides validating the present method, figure 2 reveals that the convection velocity at each wall distance depends on the wavelength. Although this dependence is not monotonic, it seems clear that longer wavelengths propagate faster than shorter ones near the wall, where $\Delta c > 0$, and that this trend is inverted far from the wall, where $\Delta c < 0$.

The general behaviour of the convection velocity near the wall is shown in figure 3(*a*) as a function of both wavelengths. Since these two-dimensional data are noisy, they have been smoothed before plotting by averaging them over logarithmic bands of width $\Delta \log \lambda \approx 1.47$ for both wavelengths (using a Fibonacci-like sequence to avoid interpolation over non-integer indices). The largest deviations of c_u from the local mean velocity are restricted to the spectral region $\lambda_x/h \geqslant 2$ and $\lambda_z/h \geqslant 0.4$, which is marked in the figure. These wavelengths coincide with the 'global modes' first identified by Bullock, Cooper & Abernathy (1978), and more recently by del Álamo & Jiménez (2003) and del Álamo *et al.* (2004), as outer layer structures penetrating into the near-wall region. For example, del Álamo & Jiménez (2003) reported that the Fourier modes of u associated to those wavelengths are strongly correlated between $y^+ = 15$ and $y = 0.5h$, and Hoyas & Jiménez (2006) showed that the long-wavelength tail of the spectral energy density of u in the near-wall region, also seen in the figure, is a reflection of spectral structures coming far from the wall.

Figure 3(*b*) displays the coherence coefficient γ_u for the same data, which is only high in the region of the global modes. Its general behaviour outside this 'global' peak is that $\gamma_u \approx 1$ only for $\lambda_z > \lambda_x$ in the sublayer ($y^+ \lesssim 5$). This geometry makes sense, because the propagation velocity has been defined with respect to x, and only those eddies that remain coherent long enough for them to move across several streamwise wavelengths appear coherent from our point of view. Eddies with $\lambda_z < \lambda_x$ have lifetimes proportional to their widths, which are shorter than their streamwise transit times. As we leave the sublayer, the coherence of these eddies drops, but the global peak remains, with maxima of the order of $\gamma_u \approx 0.25$ from the top of the

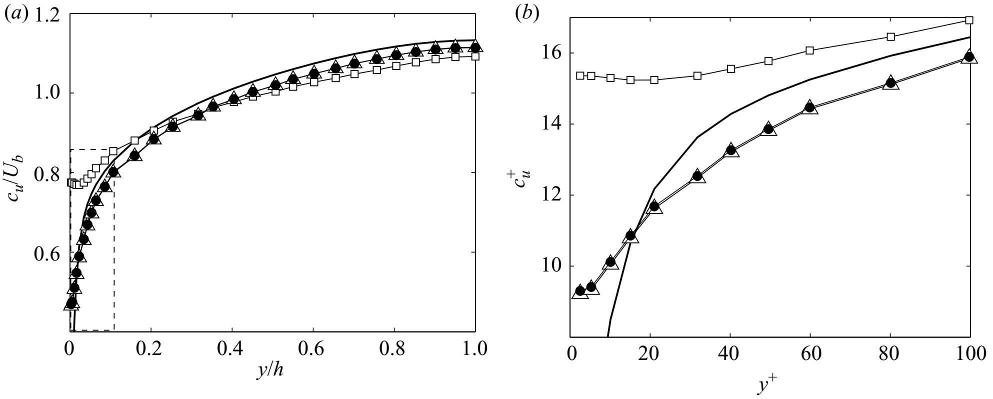

FIGURE 4. Mean turbulent convection velocity profiles of the streamwise velocity $C_u(y)$, averaged using (2.7), and plotted as a function of the wall distance. case L950. —●—, all Fourier modes included in the average; —□—, only those Fourier modes with $\lambda_x \geqslant 2h$ and $\lambda_z \geqslant 0.4h$ are included in the average ('large' wavelengths); —△—, only those Fourier modes with $\lambda_x < 2h$ and $\lambda_z < 0.4h$ are included in the average ('small' wavelengths); ———, mean velocity profile $U(y)$. (*a*) Full profile in outer units, (*b*) enlargement of the framed region in (*a*); wall units.

buffer layer to the centre of the channel. The behaviour of γ_w is roughly similar to that of γ_u, but the wall-normal velocity v is only coherent very near the wall and, interestingly, for wide global modes at the centre of the channel, where $\gamma_v \approx 1$. The convection velocities themselves are also roughly similar for the three components, but the global modes of u and w tend to move with the local mean velocity above the logarithmic layer, while the very coherent modes of v in that region retain convection velocities that correspond to layers much closer to the wall.

Figures 4(*a*) and 4(*b*) display wall-normal profiles of the convection velocity of u from case L950. These plots include velocities averaged over the whole Fourier plane, as well as those averaged over the 'large-scale' and 'small-scale' ranges defined by the two diagonal rectangles in figure 3, $(\lambda_x/h, \lambda_z/h) \geqslant (2, 0.4)$, and $(\lambda_x/h, \lambda_z/h) \leqslant (2, 0.4)$. The data show that the convection velocity of the large global modes varies relatively little with y, while the small scales follow closely the mean velocity profile, except very near the wall. The overall convection velocity is intermediate between the two, but much closer to the small-scale one, because (2.7) weights the average towards high wavenumbers. This result is consistent with the λ_x dependence of the convection velocity found in figure 2, namely that c_u increases with λ_x near the wall and decreases with λ_x away from it.

Figures 5(*a*) and 5(*b*) display profiles of C_u coming from different Reynolds numbers and averaged over the 'small' and 'large' wavelength rectangles. These data confirm the wavelength and wall-distance dependence of c_u described above, and further suggest that the convection velocity of the global modes scales roughly with the bulk mean velocity, U_b.

The constant velocity of the global modes could have been anticipated from the strong correlation observed by del Álamo & Jiménez (2003) between their near-wall and the outer layers. It is indeed easy to see that only eddies moving at similar velocities remain coherent which each other. For example, if we consider a wave,

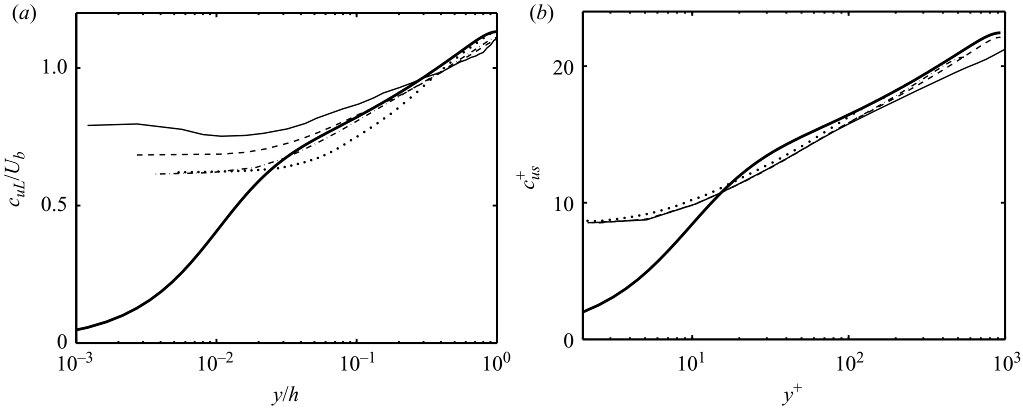

FIGURE 5. Mean convection velocity profiles of the streamwise velocity velocity $C_u(y)$ for the 'small' wavelengths and different Reynolds numbers: ········, case L180; —·—, case L550; ———, case L950; ———, case S1900. The thick solid line is the mean velocity profile from case L950. (*a*) 'large' wavelengths; (*b*) 'small' wavelengths.

$u = \exp\{ik[x - c(y)t]\}$, the correlation coefficient between $u(y)$ and $u(y')$ is

$$R(y, y') = \frac{\langle u(y)u^*(y')\rangle}{[\langle u(y)u^*(y)\rangle\langle u(y')u^*(y')\rangle]^{1/2}} = \langle \exp\{ik[c(y) - c(y')]t\}\rangle, \tag{4.1}$$

which is unity if $c(y) = c(y')$, but zero otherwise. The roughly 10 %–20 % velocity difference seen in figure 4 for the largest scales suggests that these 'global' structures should remain coherent across the logarithmic layer while being advected over 5–10 wavelengths.

The same argument implies that the convection velocity of any eddy should be constant over the range of y over which it remains coherent, and suggests that its convection velocity should be roughly the average of the mean velocity profile over some window of the order of its correlation height. The linear equivalent of this rule would be Howard's semicircle theorem in hydrodynamic stability, which states, among other things, that the propagation velocity of an eigenfunction in an inviscid parallel flow is a local average of the mean velocity profile, weighted with a particular expression of the eigenfunction norm (Drazin & Reid 1981).

Jiménez *et al.* (2004) showed that the correlation height of eddies in a channel is roughly proportional to the magnitude of their wall-parallel wavelength, and that it reaches the half-width of the channel for the global modes. This is consistent with both observations that small eddies move with the local mean velocity and that the convection velocity of the global modes is roughly proportional to the bulk velocity U_b.

Figure 6 considers the scaling of the convection velocity of u in more detail by looking at the spanwise spectral distribution of c_u at $y^+ = 15$ for different Reynolds numbers. The data have been averaged over two bands of streamwise wavelengths, separated in figure 3 by the dashed vertical line $\lambda_x = 2h$. Figures 6(*a*) and 6(*c*) show that the convection velocity of the shorter u-structures scales in wall units for all spanwise wavelengths, but not with the bulk velocity. On the other hand, figures 6(*b*) and 6(*d*) show that the convection velocity of long, wide structures scales better with U_b, consistent with figure 5(*a*). Note also that the spanwise dependence of the velocities of the longer structures collapses much better with the channel width than in wall units, confirming that, even so close to the wall, they reflect outer modes. It is

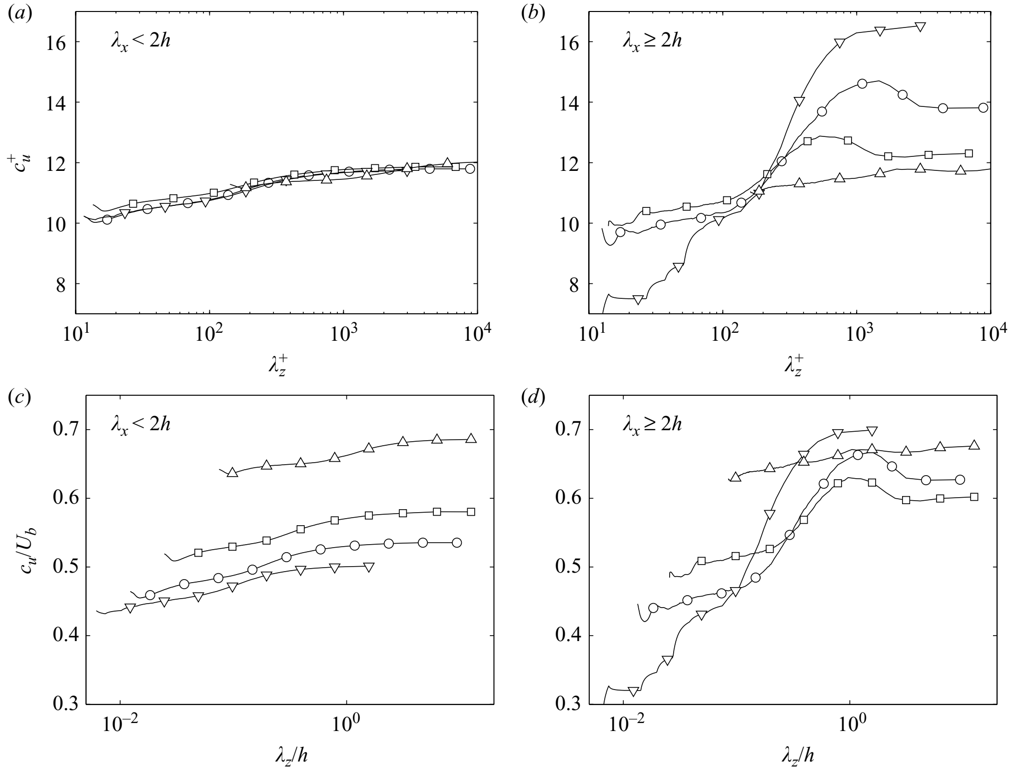

FIGURE 6. Spectral distributions of the convection velocity C_u at $y^+ = 15$, averaged for different bands of streamwise wavelength, and represented as functions of the spanwise wavelength: —△—, L180; —□—, L550; —○—, L950; —▽—, S1900. (*a*) and (*c*) are averaged over $\lambda_x < 2h$ and (*b*) and (*d*) are averaged over $\lambda_x \geqslant 2h$. (*a*) and (*b*) in wall units; (*c*) and (*d*) normalized with U_b and h.

interesting that the convection velocities reach their maxima near $\lambda_z \approx h$, and decrease again for wider structures. The same is observed at other wall distances, although it was shown by del Álamo *et al.* (2004) that u has very little energy beyond $\lambda_z \approx 2h$, and the significance of the convection velocities of such weak wide structures is unclear.

As a consequence of the observed double scaling, the separation between the convection velocity of the near-wall streaks, $c_u \approx 11u_\tau$, and that of the global modes, $c_u \approx 0.7U_b$ in the neighbourhood of the wall, increases with the Reynolds number as $U_b^+ \sim \log(Re_\tau)$. This result is clearly supported by comparing figures 6(*a*) and 6(*b*), and implies that the error committed by applying Taylor's (Taylor 1938) approximation with a wavelength-independent convection velocity can be large near the wall, and should increase with the Reynolds number. This will be discussed in detail in § 6.

Our results confirm the previous observation by Kim & Hussain (1993) that the dependence on the eddy size of the convection velocities in turbulent channels is strongest near the wall, where $U(y)$ and U_b differ most. On the other hand, we have shown that the convection velocity not only depends on λ_z, as originally reported by those authors, but also varies strongly with λ_x. Kim & Hussain (1993) computed convection velocities from $x-t$ correlations in a channel at $Re_\tau = 180$, for wavelengths shorter than $\lambda_x/h = \pi$ and narrower than $\lambda_z/h = \pi/3$. According to figure 3, these wavelengths are appropriate to capture the spanwise dependence of the convection velocity, but may be marginal to capture the streamwise one. Figure 6 also indicates that this dependence is still weak for Reynolds number considered by Kim & Hussain (1993), while it is easier to observe in the present cases L550 and L950.

In boundary layers, Krogstad *et al.* (1998) had already reported a dependence of the convection velocity on the streamwise length scale. These authors measured the convection velocity of u from two-point correlations in the laboratory at $Re_\theta = 1409$, where θ is the momentum thickness. They observed that c_u increases for streamwise separations $\Delta x \leqslant 1.5h$ in the near-wall region, while a similar increase was found for $\Delta x \leqslant 0.4h$ in the outer region. Direct comparison between the results of Krogstad *et al.* (1998) and our own is prevented by the differences in flow nature, in Reynolds numbers and between spatial separations and wavelengths. However, the same trends are observed in both sets of data except for small-scale structures near the wall, where the laboratory data might be affected by insufficient resolution.

5. A semi-empirical law for turbulent convection velocities in channels

In situations where the turbulent convection velocity has not been measured directly, such as in many experiments, or when experiments may be missing, or are still in the planning stage, it is useful to have a reasonable approximation to estimate it. Additionally, we will see below that, even when the true convection velocities are available, their use to correct the effects of Taylor's approximation (Taylor 1938) involves differentiation with respect to the wavenumber, and it is more convenient to use a smoother model than the noisier raw data.

A useful model can be derived from the previously mentioned approximation that the convection velocity is a weighted average of the mean velocity profile. This can be expressed as

$$c(\lambda_x, \lambda_z, y) \approx \int_0^{2h} U(\eta) W(y, \eta, \lambda_x, \lambda_z)\, \mathrm{d}\eta, \tag{5.1}$$

where $W(y, \eta, \lambda_x, \lambda_z)$ is a convolution window that represents statistically the wall-normal structure of eddies of wavelengths (λ_x, λ_z).

In order for (5.1) to be useful, we need an expression for the convolution window $W(y, \eta, \lambda_x, \lambda_z)$, ideally valid over a wide range of Reynolds numbers. In this section, we use a simple Gaussian model for W,

$$W(y, \eta, \lambda_x, \lambda_z, Re) = \exp\left\{ -\left[\frac{y - \eta}{H(\lambda_x, \lambda_z, Re)} \right]^2 \right\}, \tag{5.2}$$

suitably normalized to unit mass, and give an approximate expression for the window height H. We estimate H by fitting the wall-normal profile of the convection velocity of each Fourier mode of u in our channels using the Levenberg–Marquardt damped least squares iterative algorithm (Press *et al.* 2007, such as in the Matlab function lsqnonlin).

The results of the fit are presented in figure 7(*a–d*), showing a fair collapse in viscous units for the small scales, and an equally reasonable one in outer units for the larger ones. Note that case L180, which is consistently found to agree poorly with the higher Reynolds number cases, has not been included in the figure to simplify the graphics. The window height reaches its maximum, $H \approx 0.5h$, within the spectral region associated with the global modes, $\lambda_x > 2h$ and $\lambda_z \approx 2h$, which is consistent with the evidence in figure 6(*d*) that the convection velocity of the global modes scales with the bulk velocity.

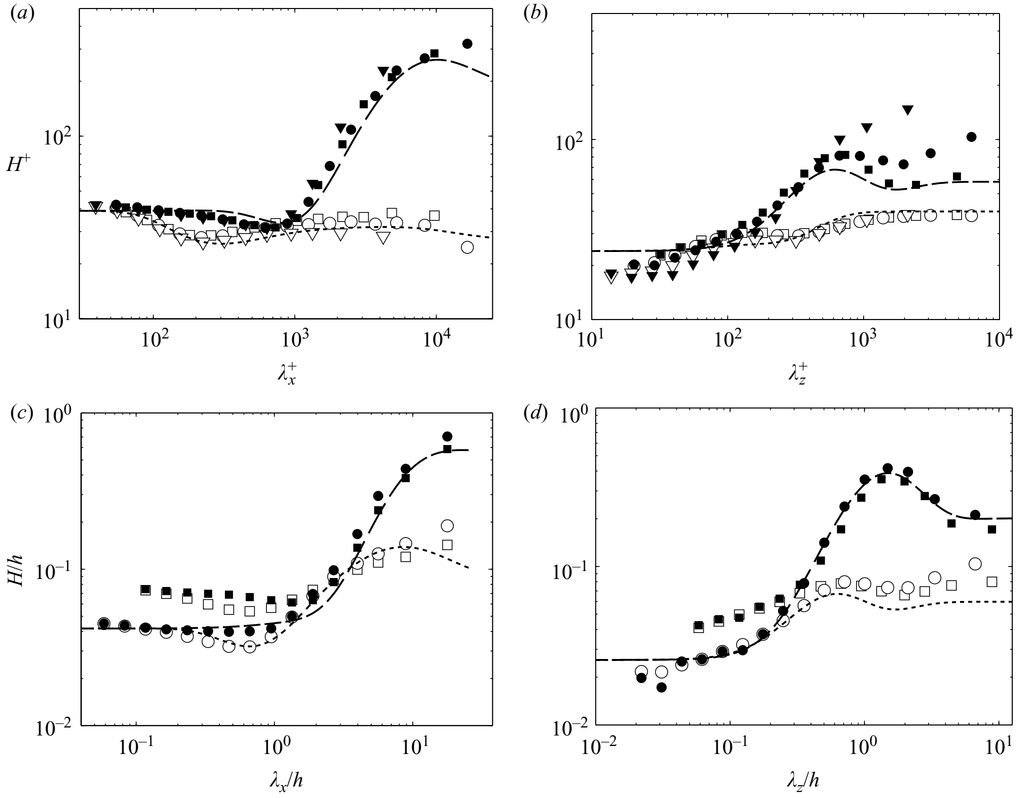

FIGURE 7. Height H of the Gaussian convolution window that transforms the mean velocity profile into convection velocities, as in (5.1)–(5.2). Symbols are the simulation data. In each panel, the open symbols and dotted line are the shorter wavelength, and solid symbols and dashed lines, the longer one. □, L550; ○, L950; ▽, S1900. The lines are defined in (5.3) for L950, with the consensus constants in table 2. (*a*) $\lambda_z^+ = 150$ and 750; (*b*) $\lambda_x^+ = 400$ and 2000; (*c*) $\lambda_z/h = 0.5$ and 2; (*d*) $\lambda_x/h = 2$ and 8.

The wavelength and Reynolds number dependence of H can be approximated by,

$$H(\lambda_x, \lambda_z, Re)/h = \frac{1}{Re_\tau}(A + Bs^4) + C\left\{\frac{27D}{4(1+D)^3}s(2-s)[1 + D(1-s)^2]^2\right\}^3 t^2, \tag{5.3}$$

where the independent variables

$$\left.\begin{aligned} s &= \tanh\left\{\frac{[1 + \lambda_x/(\Lambda_x h)]\,\lambda_z}{\lambda_x}\right\}, \\ t &= \tanh\left[\lambda_x/(\Lambda_x h)\right], \end{aligned}\right\} \tag{5.4}$$

represent respectively the isotropy and magnitude of the wavelength vector. By expressing H in terms of these variables instead of as a function of λ_x and λ_z, we were able to fit the simulation data using fewer adjustable constants. The hyperbolic tangents were introduced so that both s and t vary smoothly between 0 and 1. The length scale $\Lambda_x h$ is such that s and t become independent of λ_x when either $\lambda_x \ll \Lambda_x h$ or $\lambda_x \gg \Lambda_x h$. A similar length scale was initially considered for λ_z, but found to be unnecessary thereby reducing the number of adjustable parameters. The first term in the right-hand side of (5.3) scales in viscous units, and is bounded between A/Re_τ

case	A	B	C	D	Λ_x	E_{H1}	E_{H2}
L180	27	9	0.29	2.3	11	0.039	0.166
L550	25	13	0.57	1.3	8.4	0.030	0.041
L950	22	16	0.56	1.0	6.1	0.039	0.050
S1900	20	19	1.2	0.8	5.4	0.029	0.064
consensus	24	15	0.56	1.2	7.2	–	–

TABLE 2. Values of the dimensionless constants in expressions (5.3)–(5.4) for the height $H(\lambda_x, \lambda_z, Re)$ of the Gaussian filter used to convert $U(y)$ into $c_u(y)$. The first four rows show the optimal set of parameters to fit the empirical values of H for each numerical channel. The last one presents a 'consensus' set of constants that is recommended to estimate H at other Reynolds numbers. E_{H1} is the relative error (defined in (5.5)) of the model using the optimal set of constants for each case. E_{H2} is the relative error using the consensus constants.

and $(A+B)/Re_\tau$. The second one scales in outer units and is bounded by zero and C. The parameter D determines the value of s at which the second term of (5.3) is maximum.

We have estimated the five dimensionless parameters in (5.3)–(5.4) to fit our empirical results for $\log(H)$, using again the Levenberg–Marquardt method. Table 2 presents their estimated values for each of our channels, together with the error of the fit, defined as

$$E_H = \left[\frac{\displaystyle\int\!\!\int \log^2(H_{mod}/H_{exp})\,\mathrm{d}\log\lambda_x\,\mathrm{d}\log\lambda_z}{\displaystyle\int\!\!\int \log^2(H_{exp})\,\mathrm{d}\log\lambda_x\,\mathrm{d}\log\lambda_z} \right]^{1/2}, \tag{5.5}$$

where H_{exp} is the window height obtained from the numerical experiments and H_{mod} is the one predicted by the model. Except for the case L180, the results of the fit depend little on the Reynolds number, indicating that (5.3) is uniformly valid in the range of Reynolds numbers covered by our experiments. Note that the approximation error for case S1900 is not strictly comparable to the other three, because it has a much smaller computational box. In particular, the parameters C and D, which we have seen to be related to the magnitude and spanwise wavelength of the large-scale peak, cannot be trusted in S1900, where that wavelength $\lambda_z \approx h$ is comparable to the width of the box. The consensus parameters have been derived mostly from the two cases L550 and L950.

Figures 7(*a–d*) show that the model reproduces well the wavelength dependence of H for case L950 using the consensus set of constants. The same is true for the rest of our channels (not shown), consistent with the low values of E_{H2} given in table 2. We therefore expect that (5.3)–(5.4) could be used to estimate convection velocities at Reynolds numbers higher than those considered in our numerical experiments.

Beyond matching the convolution height, figures 8(*a*) and 8(*b*) show that the model (5.1)–(5.4), with the consensus constants in table 2, reproduces well the wall normal profiles of C_u. The plot shows profiles from two wavevectors, representative of the global modes ($\lambda_x = 5.6h$, $\lambda_z = 1.5h$, $H = 0.32h$) and of the structures of the buffer layer ($\lambda_x^+ = 620$, $\lambda_z^+ = 160$, $H^+ = 34$). In both cases, the convolution model yields an accurate estimation of $C_u(y)$, especially near the wall where the convection velocity differs substantially from $U(y)$. Away from the wall, the convection velocities obtained from (5.1)–(5.4) are systematically closer to the mean profile than the actual

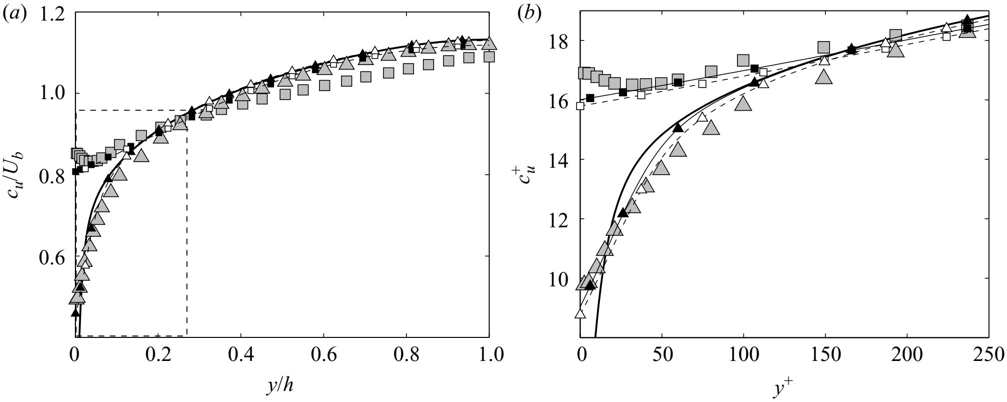

FIGURE 8. Profiles of the turbulent convection velocity $C_u(y)$ of the streamwise velocity component, as a function of the wall distance. Data from two wavelength pairs of L950; □, $(\lambda_x, \lambda_z) = (5.6,\ 1.5)h$; △, $(\lambda_x, \lambda_z) = (0.66,\ 0.18)h$, $(\lambda_x^+, \lambda_z^+) = (620,\ 160)$. Grey symbols are (2.7); —▲—and —■—, convolution (5.1)–(5.4) of the measured velocity profile, using the consensus constants in table 2. – – △ – – and – – □ – –, using Cess approximation for the mean velocity profile. ———, mean velocity profile. (*a*) Full profiles in outer units, (*b*) enlargements of the framed region in (*a*); wall units.

ones, but they still reproduce correctly the trend of the wavelength dependence. The approximation error could be decreased by considering asymmetric windows with longer tails towards the wall, but we have preferred to keep the functional form of the filter in (5.2) as simple as possible.

Note that all the advection velocities converge approximately to $U(y)$ above $y/h \approx 0.15$, which agrees with the evidence in Dennis & Nickels (2008) that the spatial velocity field at that height can be reconstructed from temporal hot wire data. On the other hand, the present data suggest that the same might not be true closer to the wall.

Figures 8(*a*) and 8(*b*) also include estimations of $C_u(y)$ obtained by applying (5.1) to the mean profile from the Cess approximation (Cess 1958), instead of the measured one. For reference, that approximation is based on the total (molecular plus eddy) viscosity,

$$\frac{\nu_{tot}}{\nu} = \frac{1}{2}\left\{1 + \frac{K^2 Re_\tau^2}{9}[2Y - Y^2]^2[3 - 4Y + 2Y^2]^2\left[1 - \exp\left(\frac{-Y Re_\tau}{A}\right)\right]^2\right\}^{1/2} + \frac{1}{2}, \tag{5.6}$$

where $Y = y/h$, with constants $A = 25.4$ and $K = 0.426$ for turbulent channels over a wide range of Reynolds numbers (del Álamo & Jiménez 2006). The mean velocity is obtained by integrating the mean momentum equation $\partial_y U = (1 - Y)u_\tau^2/\nu_{tot}(Y)$. As expected, the profiles of C_u obtained from this profile are nearly identical to those obtained by filtering the true $U(y)$.

6. The effect of Taylor's approximation

We now examine the errors introduced in the energy spectra by applying Taylor's approximation (Taylor 1938) with a wavelength-independent advection velocity. It is clear from figure 3 that this analysis requires two-dimensional spectral information, because the convection velocity depends on both the streamwise and spanwise wavelengths.

The one-dimensional wavenumber spectrum is derived from the two-dimensional one by integration with respect to k_z,

$$E(k_x) = \int E(k_x, k_z)\, \mathrm{d}k_z, \tag{6.1}$$

and the same is true for the one-dimensional frequency spectrum

$$E(\omega) = \int E(\omega, k_z)\, \mathrm{d}k_z \tag{6.2}$$

in terms of the two-dimensional $\omega - k_z$ spectrum. Neglecting errors unrelated to the variable convection velocity, we can define a 'corrected' Taylor wavenumber for a given passing frequency, $k_x = \omega/c_u$, and an 'uncorrected' one, $k_{x,T} = \omega/U(y)$, with corresponding definitions for the wavelengths. Expressed as a function of $k_{x,T}$, (6.2) becomes the 'uncorrected' Taylor spectrum,

$$E_T(k_x) = U(y)E(\omega). \tag{6.3}$$

The direct 'Taylor correction' problem would be to estimate a 'corrected' approximation to $E(k_x)$ starting from $E(\omega, k_z)$,

$$E(k_x) = \int E[\omega(k_x, k_z), k_z]\, |\mathrm{d}\omega/\mathrm{d}k_x|\, \mathrm{d}k_z, \tag{6.4}$$

where the integral is taken along paths of constant streamwise wavenumber in the mixed Fourier plane. The factor $|\mathrm{d}\omega/\mathrm{d}k_x|$ is the Jacobian of the transformation between ω and k_x, and ensures that the energy of an eddy is the same in both representations, $E(\omega)|\mathrm{d}\omega| = E(k_x)|\mathrm{d}k_x|$.

Because two-dimensional $\omega - k_z$ spectra are seldom compiled in laboratory experiments, it is difficult to directly estimate 'Taylor corrections' to laboratory spectra even if (5.1)–(5.4) provide an approximation for $|\mathrm{d}\omega/\mathrm{d}k_x|$. Therefore, we will focus on the 'inverse' problem of estimating the uncorrected spectrum (6.2)–(6.3), which is the output of most experiments, from the two-dimensional wavenumber spectrum $E(k_x, k_z)$, which is available from simulations. The result will then be compared with one-dimensional experimental frequency spectra, to try to separate which of their features correspond to properties of the underlying spatial spectra, and which ones are artifacts of the transformation.

From the definition of passing frequency, the 'corrected' frequency spectrum can be written as

$$E(\omega) = \int E[k_x(\omega, k_z), k_z]\, |\mathrm{d}k_x/\mathrm{d}\omega|\, \mathrm{d}k_z, \tag{6.5}$$

where the integral is taken along paths of constant frequency in the wavenumber plane.

For pre-multiplied spectra, (6.5) becomes

$$\omega E(\omega) = k_x E_T(k_x) = \int k_x E[k_x(\omega, k_z), k_z]\, J(k_x, k_z)\, \mathrm{d}k_z, \tag{6.6}$$

where

$$J = (\omega/k_x)\, |\mathrm{d}k_x/\mathrm{d}\omega| \tag{6.7}$$

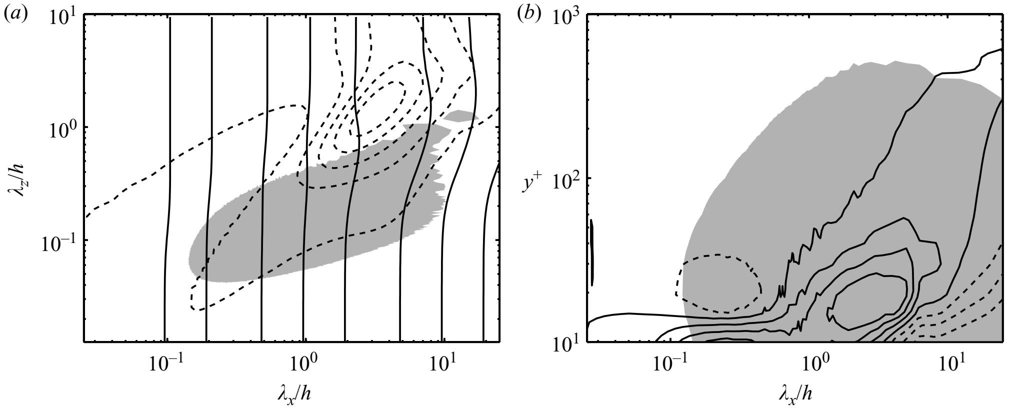

FIGURE 9. case L950. (*a*) $y^+ = 15$. The shaded area is the pre-multiplied two-dimensional spectrum of u, above 0.2 times its maximum in that plane. Solid lines are constant frequency isocontours, corresponding to uncorrected Taylor wavelengths. Each contour is given approximately by its intersection with the horizontal axis. Dashed lines are isocontours of the mapping factor (6.7), $J = 1(0.1)1.4$. (*b*) The shaded area is the pre-multiplied one-dimensional spectrum of u, above 0.2 times its maximum at any height. Isocontours are the relative correction (6.8) to the one-dimensional pre-multiplied spectrum due to Taylor's approximation. Contours are $-0.3(0.1)0.3$; dashed lines are negative.

is a dimensionless version of the mapping factor, which can be recognized as the ratio between the phase and the group velocities. It can be considerably different from unity if the advection velocity changes rapidly with the wavenumber.

This behaviour is shown in figure 9(*a*), which displays the same buffer-layer plane used for figure 3. The general location of the u-spectrum is shown shaded for reference, and the solid lines are contours of constant $k_{x,T}$. They spread out near the short-wavelength edge of the global modes, because the global wavelengths to the right of that limit are aliased to higher frequencies (or to shorter uncorrected wavelengths) by their higher convection velocities. Where the isofrequency lines diverge, the mapping factor increases because the energy is crowded into a narrower frequency interval. The overall effect of J is to damp the frequency spectrum at intermediate and long wavelengths, and to augment it near $\lambda_x/h = O(1)$, where the advection velocity changes from $U(y)$ to U_b. The magnitude of this change depends on $U(y) - U_b$, and is therefore expected to be strongest in the buffer and deep logarithmic layers, where it may create artificial maxima or minima in $E_T(k_x)$. The maximum of J in figure 9(*a*) is 1.5, although its influence on the integral (6.6) is not as large because it is located in a region of relatively low energy.

The effect on the one-dimensional spectrum is shown in figure 9(*b*), which contains the difference between the pre-multiplied wavenumber spectrum and its uncorrected Taylor counterpart

$$k_x \frac{E_T(k_x, y) - E(k_x, y)}{\max_{k_x}[k_x E(k_x, y)]}, \tag{6.8}$$

given as a function of the streamwise wavelength and of the wall distance. The location of the spectrum is again shaded for reference, and the magnitude of the correction is normalized at each y by the maximum of the pre-multiplied spectrum at that height. It is seen that the relative errors are highest near the wall, but that they remain of the order of 10 % at the lower edge of the logarithmic layer. As it moves

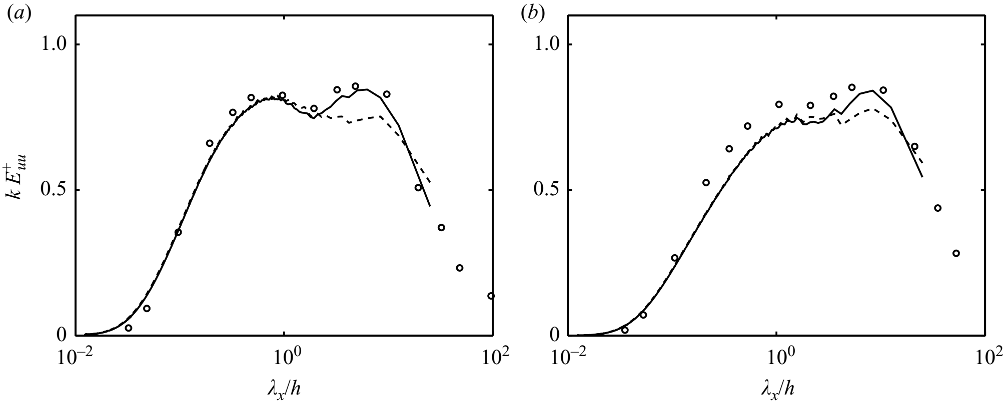

FIGURE 10. One-dimensional pre-multiplied energy spectra, $k_x E_{uu}(k_x)$. ○, Perry & Abell (1975), $Re_\tau = 2325$. Lines are case (Hoyas & Jiménez 2006): – – –, true wavelengths; ——, uncorrected Taylor wavelengths. (a) $y^+ = 100$, (b) $y^+ = 200$.

away from the wall, the maximum of the correction drifts from $\lambda_x \approx h$ to the longer wavelengths characteristic of the global modes, and its effect could easily be mistaken for energy from the outer modes penetrating into the buffer region. This spurious accumulation of energy should disappear above the wall distance where $U(y) \approx U_b$, which in channels is located near the top of the logarithmic layer, $y \approx 0.3h$. In our simulations, the convection velocities become very similar to the local mean velocity above $y \approx 0.15h$, but, as we have already mentioned, the intensity of the corrections should increase with the Reynolds number.

It should be noted that figure 9 has been computed using the approximate mapping in § 5, rather than the measured convection velocities, which are too noisy for differentiation.

Bimodal spectra have often been documented near the wall, perhaps first emphasized by Hites (1997) in boundary layers. Using those data, Jiménez & Hoyas (2008) noted that the outer energy peak in experimental boundary layers extends closer to the wall than in numerical channels, although they cautioned that this could be due in part to the difference between wavenumber and frequency spectra. A similar peak near the wall was observed in experimental boundary layers by Kunkel (2003) and by Kunkel & Marusic (2006) and Monty & Chong (2008) have noted recently that a broad long-wavelength peak is present near the wall in experimental channels, but not in numerical ones.

That outer structures extend into the buffer layer has been well documented in simulations, independently of Taylor's approximation (Hoyas & Jiménez 2006), and is not in doubt, but the pre-multiplied long-wave spectra in those cases tend to be flat, rather than bimodal, consistent with the theoretical arguments for a k_x^{-1} spectrum (Townsend 1976, pp. 150–158). In view of the previous arguments, it is fair to ask whether the bimodal nature of the experimental spectra might be partly an artifact of the Taylor approximation.

This hypothesis is tested in figure 10. We are not aware of any published experimental spectra of channels at Reynolds numbers similar to our simulations, and external and internal flows are different enough to make a direct comparison difficult (Jiménez & Hoyas 2008). We have therefore used older spectra for pipes (Perry & Abell 1975), which also display the peak in question. The figure contains the experimental data reduced to wavelengths using the local mean velocity, the true wavelength spectrum for the channel, and the channel spectrum reduced to uncorrected Taylor wavelengths using (6.6). The appearance of a long-wavelength peak due to Taylor's approximation is obvious, and matches quantitatively the uncorrected experimental spectrum in the $y^+ = 100$ case. The experimental spectrum at $y^+ = 200$ is generally higher than in the simulation, corresponding to the higher turbulent intensity measured in that experiment at that point. The reason for that is unknown, and could be a difference between pipes and channels. In addition, Perry & Abell (1977) concluded that their original data had been measured too close to the pipe entrance to be in equilibrium, which would probably be more noticeable far from the wall. Even so, the Taylor correction to the channel spectrum, although smaller than closer to the wall, is still clear.

7. Conclusions

Taylor's (Taylor 1938) abstraction of turbulent flows as fields of frozen eddies advected by the mean flow has played a major role in turbulence research. Numerous methods have been developed to determine turbulent convection velocities, which are often used in laboratory experiments to infer the spatial organization of turbulence from temporal series of measurements. However, the vast majority of them are of limited use, because they require the prior determination of the frequency–wavenumber spectrum, which is rather laborious.

We have presented a new method to compute the turbulent convection velocities of single Fourier modes, which is based on ensemble averages of their time derivatives, and therefore does not require the knowledge of the frequency–wavenumber spectrum. This convection velocity minimizes the variance of the total advective derivative of each mode, suggesting a natural extension of its definition to groups of modes, or even to complete flow fields. When used on numerical simulations, where the time derivative can be computed directly from the Navier–Stokes equations, it provides quantitative information on the influence of each term of the momentum equation on the flow dynamics.

The new method has been related analytically to existing ones that search for maxima in the frequency–wavenumber spectrum (surveyed by Hussain & Clark 1981; Goldschmidt *et al.* 1981). It is found that the present convection velocity is equivalent to $c = \omega_0/k_x$, where ω_0 is the location of the centre of gravity of the spectrum for constant wavenumber. Based on these results, we have proposed variations of the definition of the convection velocity in terms of the temporal spectrum of the streamwise derivatives, which could be more practical for laboratory experiments. The present method has also been shown empirically to agree well with older ones in a numerical channel at $Re_\tau = 550$.

We have used the new scheme to determine convection velocities in computational channels with Reynolds numbers $180 \leqslant Re_\tau \leqslant 1900$, and to characterize their dependence on the streamwise and spanwise wavelength, and on the wall distance. The smallest eddies follow the local mean velocity everywhere except near the wall, but the convection velocity becomes more uniform in y with increasing wavelength, and eddies with $\lambda_x \geqslant 2h$ and $\lambda_z \geqslant 0.4h$ travel at almost uniform speeds, close to the bulk velocity. These eddies correspond to the 'global' modes identified from cross-stream correlations in previous investigations (Bullock *et al.* 1978; del Álamo & Jiménez 2003; del Álamo *et al.* 2004). In fact, having a uniform convection velocity is a necessary condition for a Fourier mode to be correlated across the channel height.

Since the new method can be expressed as a minimization problem, it automatically provides a measure of the goodness of the frozen-turbulence approximation as a function of wavelength and position. Interestingly, the only eddies that can be approximately described as frozen waves are short-wide ones in the viscous sublayer, and the global modes.

The results of this study support the idea that the convection velocity of an eddy is closely related to its height (Townsend 1976, pp. 26–27). Based on it, we have constructed an empirical formula that approximates the convection velocity of a Fourier mode as the convolution of the mean velocity profile with a Gaussian window. Although no particular effort was made to tune the window, the resulting approximation agrees well with the measured convection velocities over the whole range of available two-dimensional wavelengths, wall distances and Reynolds numbers. The agreement is particularly good near the wall, where the convection velocity differs most from the mean profile, and persists even when the exact velocity profile is substituted by a reasonably good approximation, such as in Cess (1958).

We propose that this model can be used to correct the errors introduced by applying Taylor's frozen-turbulence approximation (Taylor 1938) in experimental data with a convection velocity that does not depend on eddy size. Estimating those errors requires, however, previous knowledge of the ($\omega - k_z$) dependence of the spectrum, which is limited in laboratory experiments. Therefore, we have estimated them using data from numerical simulations. The thus estimated errors can be considerable. Not only are the large scales aliased into shorter ones near the wall, but the shape of the spectrum changes, creating a spurious spectral peak near the short-wavelength limit of the global modes, essentially because the energy is squeezed into a local maximum by the differential deformation of the wavenumber range. The error is larger in the buffer and inner logarithmic layers, and increases with the Reynolds number. Such maxima have been reported in experiments, but a quantitative comparison of the Taylor-corrected channel data with experimental data from pipes suggests that they may be, at least in part, artifacts of the incorrect application of the frozen-turbulence approximation.

One of the consequences of these artefactual peaks is that the true wavenumber spectrum of turbulence near walls may be closer to the k_x^{-1} prediction of Townsend (Townsend 1976, pp. 150–158) than concluded in recent experiments. A full discussion of this point is beyond the scope of this paper, but some preliminary considerations might be in order. The argument for the k_x^{-1} spectrum appears robust, as it is simply based on having a single scale for the velocity fluctuations (usually u_τ) and no scale for the lengths (see Nickels *et al.* 2007, for a recent review). However, the experimental observation of k_x^{-1} spectra has been elusive (Hites 1997; Morrison *et al.* 2002; del Álamo *et al.* 2004) mainly because its expected range is found to overlap the long-wavelength maximum mentioned above. In view of the present results, some of those data may have to be reconsidered.

Even more interesting are the theoretical implications of that reconsideration. To explain the absence of the expected spectral behaviour, it has been suggested that the largest scales may not scale with u_τ, but with some outer velocity such as U_b (Morrison *et al.* 2002; del Álamo *et al.* 2004; Jiménez & Hoyas 2008). This velocity follows reasonably well the Re_τ scaling of the large-scale spectral peak, but the correction discussed above would yield a similar scaling at a given y^+, because it is proportional to the difference between U_b and the local mean velocity.

A related question is the observed scaling of the velocity fluctuation intensities in the logarithmic layer at constant y/h, which grow logarithmically with the Re_τ instead of collapsing in wall units (Hoyas & Jiménez 2006; Jiménez & Hoyas 2008). This behaviour has been argued to result from the integrated energy of the long-wavelength peak, because it is not observed when considering scales shorter than a few boundary-layer thicknesses (del Álamo *et al.* 2004; Jiménez 2007). This explanation might also have to be substituted by an alternative one. A possible argument to explain that the large-scale end of the spectrum has increasing energy with Re_τ while keeping a constant intensity, may be that it gets longer even when expressed in terms of the boundary-layer thickness. Although this idea might appear strange, it does not contradict experimental evidence, since Jiménez & Hoyas (2008) showed that most published high-Reynolds-number spectra are too short to have a definite long-wavelength limit. In fact, it is even theoretically plausible, because the eddy-turnover time of a large structure is of the order h/u_τ, during which time it is advected, and sheared, over distances of order $U_b h/u_\tau \sim h Re_\tau$. Again, this question cannot be analysed rigorously in the present paper, but it emphasizes the importance of either higher Reynolds number simulations, or of long experimental two-dimensional $\omega - k_z$ spectra.

This work was supported in part by the CICYT grant TRA2006-08226. Juan C. del Álamo was partially supported by consecutive FPU and Fulbright fellowships from the Spanish Ministry of Education.

REFERENCES

del Álamo, J. C. & Jiménez, J. 2002 Characteristics of scalar dispersion in turbulent-channel flow. In *Proceedings of Summer Program* (ed. Parviz Moin, Nagi N. Mansour & Peter Bradshaw), pp. 203–214. Center for Turbulence Research, Stanford University.

del Álamo, J. C. & Jiménez, J. 2003 Spectra of the very large anisotropic scales in turbulent channels. *Phys. Fluids* **15**, L41–L44.

del Álamo, J. C. & Jiménez, J. 2006 Linear energy amplification in turbulent channels. *J. Fluid Mech.* **559**, 205–213.

del Álamo, J. C., Jiménez, J., Zandonade, P. & Moser, R. D. 2004 Scaling of the energy spectra of turbulent channels. *J. Fluid Mech.* **500**, 135–144.

del Álamo, J. C., Jiménez, J., Zandonade, P. & Moser, R. D. 2006 Self-similar vortex clusters in the logarithmic region. *J. Fluid Mech.* **561**, 329–358.

Bullock, K. J., Cooper, R. E. & Abernathy, F. H. 1978 Structural similarity in radial correlations and spectra of longitudinal velocity fluctuations in pipe flow. *J. Fluid Mech.* **88**, 585–608.

Capon, J. 1969 High-resolution frequency–wavenumber spectrum analysis. *Proc. IEEE* **57** (8), 1408–1418.

Cess, R. D. 1958 A survey of the literature on heat transfer in turbulent tube flow. *Tech. Rep.* Report 8-0529-R24. Westinghouse Research.

Choi, H. & Moin, P. 1990 On the space–time characteristics of wall-pressure fluctuations. *Phys. Fluids* A **2**, 1450–1460.

Comte-Bellot, G. & Corrsin, S. 1971 Single eulerian time correlation of full and narrow band velocity signals in grid-generated ‘isotropic’ turbulence. *J. Fluid Mech.* **48**, 273–337.

Dennis, D. J. & Nickels, T. B. 2008 On the limitations of Taylor’s hypothesis in constructing long structures in a turbulent boundary layer. *J. Fluid Mech.* **614**, 197–206.

Drazin, P. G. & Reid, W. H. 1981 *Hydrodynamic Stability*. Cambridge University Press.

Fisher, M. J. & Davies, P. O. A. L. 1963 Correlation measurements in a non-frozen pattern of turbulence. *J. Fluid Mech.* **18**, 97–116.

Flores, O. & Jiménez, J. 2006 Effect of wall-boundary disturbances on turbulent channel flows. *J. Fluid Mech.* **566**, 357–376.

Goldschmidt, V. W., Young, M. F. & Ott, E. S. 1981 Turbulent convective velocities (broadband and wavenumber dependent) in a plane jet. *J. Fluid Mech.* **105**, 327–345.

Hites, M. 1997 Scaling of high-Reynolds number turbulent boundary layers in the national diagnostic facility. PhD thesis, Illinois Institute of Technology, Chicago, IL.

Hoyas, S. & Jiménez, J. 2006 Turbulent channel simulation at $re_\tau = 2000$. *Phys. Fluids* **18**, 011702.

Hussain, A. K. M. F. & Clark, A. R. 1981 Measurements of wavenumber-celerity spectrum in plane and axisymmetric jets. *AIAA J.* **19**, 51–55.

Jiménez, J. 2007 Recent developments in wall-bounded turbulence. *Rev. R. Acad. Cien. Ser.* A*, Mat.* **101**, 187–203.

Jiménez, J., del Álamo, J. C. & Flores, O. 2004 The large-scale dynamics of near-wall turbulence. *J. Fluid Mech.* **505**, 179–199.

Jiménez, J. & Hoyas, S. 2008 Turbulent fluctuations above the buffer layer of wall-bounded flows. *J. Fluid Mech.* **611**, 215–236.

Kim, J. & Hussain, F. 1993 Propagation velocity of perturbations in turbulent channel flow. *Phys. Fluids* **6**, 695–706.

Krogstad, P. A., Kaspersen, J. H. & Rimestad, S. 1998 Convection velocities in a turbulent boundary layer. *Phys. Fluids* **10** (4), 949–957.

Kunkel, G. J. 2003 An experimental study of the high Reynolds number boundary layer. PhD thesis, Aerospace Engineering and Mechanics, University of Minnesota, Minneapolis, MN.

Kunkel, G. J. & Marusic, I. 2006 Study of the near-wall-turbulent region of the high-Reynolds-number boundary layer using atmospheric data. *J. Fluid Mech.* **548**, 375–402.

Monty, J. & Chong, M. 2008 Comparing experimental and direct numerical simulation results from a turbulent channel flow. In *Proceedings of the 61st Annual Meeting Division of Fluid Dynamics*, EB-10. American Physical Society.

Morrison, J. F., Jiang, W., McKeon, B. J. & Smits, A. J. 2002 Reynolds number dependence of streamwise velocity spectra in turbulent pipe flow. *Phys. Rev. Lett.* **88**, 214501.

Nickels, T. B., Marusic, I., Hafez, S., Hutchins, N. & Chong, M. S. 2007 Some predictions of the attached eddy model for a high Reynolds number boundary layer. *Phil. Trans. R. Soc.* A **365**, 807–822.

Perry, A. E. & Abell, C. J. 1975 Scaling laws for pipe-flow turbulence. *J. Fluid Mech.* **67**, 257–271.

Perry, A. E. & Abell, C. J. 1977 Asymptotic similarity of turbulence structures in smooth- and rough-walled pipes. *J. Fluid Mech.* **79**, 785–799.

Press, W. H., Teukolsky, S. A., Vetterling, W. T. & Flannery, B. P. 2007 *Numerical Recipes. The Art of Scientific Computing*, 3rd edn. Cambridge University Press.

Taylor, G. I. 1938 The spectrum of turbulence. *Proc. R. Soc. Lond.* **164** (919), 476–490.

Townsend, A. A. 1976 *The Structure of Turbulent Shear Flows*, 2nd edn. Cambridge University Press.

Willmarth, W. W. & Wooldridge, C. E. 1962 Measurements of the fluctuating pressure at the wall beneath a thick turbulent boundary layer. *J. Fluid Mech.* **14** (2), 187–210.

Wills, J. A. B. 1964 On convection velocities in turbulent shear flows. *J. Fluid Mech.* **20**, 417–432.

Zaman, K. B. M. Q. & Hussain, A. K. M. F. 1981 Taylor hypothesis and large-scale coherent structures. *J. Fluid Mech.* **112**, 379–396.